KSUPT-01/6 October 2001

Galactic Foregrounds in OVRO and UCSB South Pole 1994 Cosmic Microwave Background Anisotropy Data

Pia Mukherjee[1], Brian Dennison[2], Bharat Ratra[1], John H. Simonetti[2], Ken Ganga[3], and Jean-Christophe Hamilton[4,5]

ABSTRACT

We study Galactic emission foreground contamination of the OVRO and UCSB South Pole 1994 cosmic microwave background (CMB) anisotropy data by cross-correlating with templates of infrared dust emission and new high resolution H_α data. H_α data provide rough upper limits on the level of free-free emission in the data sets. The cross-correlation analysis does not contradict a two component foreground emission hypothesis, with the two dust-correlated components being free-free emission and spinning dust emission.

Subject headings: cosmology: observation — cosmic microwave background — diffuse radiation — ISM: dust, extinction

1. Introduction

Cosmic microwave background (CMB) observations have begun to provide interesting constraints on cosmological parameters (see, e.g., Ratra et al. 1999a; Rocha et al. 1999; Knox & Page 2000; Wang & Mathews 2000; Podariu et al. 2001; Netterfield et al. 2001; Pryke et al. 2001; Stompor et al. 2001). To determine high precision constrains on cosmological parameters from CMB anisotropy data, it must be carefully cleaned of any contaminating foregrounds to extract purely cosmological fluctuations to high accuracy.

[1]Department of Physics, Kansas State University, Manhattan, KS 66506; pia, ratra@phys.ksu.edu.

[2]Martin Observatory, Institute for Particle Physics and Astrophysics, and Department of Physics, Virginia Polytechnic Institute and State University, Blacksburg, VA 24061; dennison@astro.phys.vt.edu, jhs@vt.edu.

[3]Infrared Processing and Analysis Center, California Institute of Technology, Pasadena, CA 91125; kmg@ipac.caltech.edu.

[4]Physique Corpusculaire et Cosmologie, Collège de France, 11 Place Marcellin Berthelot, 75231 Paris, France.

[5]Institut des Sciences Nucléaires, 53 Av. des Martyrs, 38026 Grenoble, France; hamilton@in2p3.fr.

So far the main sources of diffuse Galactic microwave emission known to be present are thermal dust, synchrotron, and free-free. The identification and removal of free-free emission is not straightforward as it is likely to dominate the other two sources only in a small range of frequencies where total Galactic emission is minimal. Thus unlike the other two foregrounds it cannot be traced by observing at much higher or lower frequencies. However, Galactic H_α line emission, which is produced by the same warm ionized medium (WIM) responsible for free-free emission, can be a good tracer of free-free emission at high Galactic latitudes where there is expected to be minimal extinction from dust. Recently it has been proposed that there is at least indirect evidence for the presence of another component of Galactic emission, spinning dust emission from rotationally excited small dust grains. The idea of rotational emission from dust grains is being more actively pursued after the discovery of a substantial population of ultra-small dust grains (Ferrara & Dettmar 1994). The model of Draine & Lazarian (1998a,b) predicts a microwave emission spectrum for this component that peaks at low frequencies ($\sim 10-30$ GHz), with details of the spectrum, such as the location of the peak, dependent on the properties of the dust grains and their environment.

Schlegel, Finkbeiner, & Davis (1998) have begun an effort of making available high quality tracers of thermal dust emission, which peaks at about 3000 GHz, as well as maps of infrared (hereafter IR) emission at frequencies higher than this, emission that is expected to have been produced thermally by very small dust grains. They (Finkbeiner & Davis, in preparation) and others (Lawson et al. 1987) have also worked on cleaning and destriping the 408 MHz (Haslam et al. 1981) map of synchrotron emission and on creating a map of the spatial variation in the synchrotron spectral index based on the 408 MHz, 1420 MHz (Reich & Reich 1986), and 2326 MHz (Jonas, Baart, & Nicholson 1998) radio surveys (Finkbeiner & Davis, in preparation). New observations are being made by the Galactic Emission Mapper[6] (GEM) project. Full sky maps of H_α emission are becoming available (the Southern H_α Sky Survey or SHASSA[7], the Wisconsin H_α Mapper or WHaM[8], and the Virginia Tech Spectral-Line Survey or VTSS[9]).

In order to assess the level of Galactic emission contamination in CMB anisotropy data, the available maps of Galactic emission can be used as spatial templates of Galactic emission structure and one may cross-correlate CMB data with such maps. When CMB data sets have sufficient frequency coverage and high signal-to-noise, a spectral analysis of this data alone can in principle distinguish foregrounds from the CMB signal. However, spatial variation in the spectral indices of the foreground emission components and the uncertain spectral shape of the proposed spinning dust component introduce complications.

So far, regarding microwave-IR correlations, estimates of the correlation slope a (defined in §

[6]http://aether.lbl.gov/

[7]http://amundsen.swarthmore.edu/SHASSA/

[8]http://www.astro.wisc.edu/wham/

[9]http://www.phys.vt.edu/vtss

3) between 100 μm emission and microwave emission obtained from DMR (Kogut et al. 1996a,b), 19 GHz (de Oliviera-Costa et al. 1998), Saskatoon (de Oliviera-Costa et al. 1997), OVRO (Leitch et al. 1997, along with this work), UCSB South Pole 1994 (Hamilton & Ganga 2001) and Tenerife (de Oliviera-Costa et al. 1999; Mukherjee et al. 2001, Galactic emission correlations are not found at high Galactic latitudes like $b > 30^\circ$) observations are such that they are roughly consistent with a free-free emission spectral index over this wide range of frequencies (10−90 GHz) and angular scales (7° to $7'$). MAX 4 data show some IR correlation at 100 GHz in one field (Lim et al. 1996; Ganga et al. 1998). No IR correlations were found in the Python V (Coble et al. 1999) or QMAP (de Oliviera-Costa et al. 2000) data. If the component that correlates with the IR dust continuum has similar scale dependence as IR dust emission itself (which has a multipole space power spectrum $\propto \ell^{-3}$, Kogut et al. 1996b), then this relation will be independent of scale[10].

However, if this correlated emission were really free-free emission, then a similar correlation should exist between H_α and IR emission. The relation between free-free and H_α emission is

$$T_{\rm ff} \sim 7\ \mu{\rm K} \left(\frac{T}{10^4\ {\rm K}}\right)^{0.55,0.85} \left(\frac{\lambda}{1\ {\rm cm}}\right)^{2.1} \left(\frac{I_{H_\alpha}}{\rm R}\right), \tag{1}$$

at wavelength λ, where $T_{\rm ff}$ is the brightness temperature for free-free emission, I_{H_α} is the intensity of H_α emission, and the power law index on the gas temperature changes from 0.55 for temperature $T \leq 2.6 \times 10^4$ K to 0.85 for $T > 2.6 \times 10^4$ K. The assumptions that go into deriving this relation include a fraction of singly ionized helium of unity, a helium to hydrogen ratio of 0.08, an approximate expression for the Gaunt factor, and further the relation is valid only for lines of sight in which interstellar extinction is negligible (Reynolds & Haffner 2000). Regarding H_α-IR correlations, it has been found so far that they are only marginal. Correlation slopes obtained (Kogut 1997; McCullough 1997; Reynolds et al. 1995) are a factor of two or three lower than what is expected based on the microwave-IR correlation slopes and have significant uncertainties at present. Based on microwave-IR correlations, assuming that what correlates is free-free, and given the relation between free-free and H_α emission, $\Delta I_{H_\alpha}/\Delta I_{100\mu m} \approx 2$ R(MJy/sr)$^{-1}$ is expected, where ΔI refers to fluctuations in the intensity of the corresponding emission component. What is observed is something like 0.8 R(MJy/sr)$^{-1}$, at low significance, on small patches of sky in the North Celestial Pole (NCP) region and in places in the southern Galactic hemisphere. H_α maps covering large areas of the sky will provide valuable information. However, if the microwave-IR correlation is only in part due to free-free emission, then this value may be acceptable. This ratio may also vary across the sky due to the variation in optical extinction along different lines of sight. See Smoot (1998), Bartlett & Amram (1998), McCullough et al. (1999), Valls-Gabaud (1998), Kogut (1999), and Draine & Lazarian (1999) for reviews of the relation between H_α and free-free emission and for discussions of how spinning dust emission might be responsible for the "anomalous" IR-correlated emission.

[10]Bartlett & Amram (1998) point out that such a power spectrum implies that the true sky variance remains roughly constant towards small scales, but estimates of this variance in restricted patches of sky may be "pulled" far from the true variance by important correlations on scales of the patch size.

Here we study microwave data from the OVRO (RING5M) and UCSB South Pole 1994 (hereafter SP94) CMB anisotropy experiments. The OVRO observations consist of 36 fields around the NCP, at a declination of $\sim 88^\circ$, at frequencies of 14.5 and 31.7 GHz, with a double differencing $7'$ FWHM beam (see Leitch et al. 2000 for more information on the OVRO experiment). When the observed data are modelled as consisting of a CMB component and a single foreground of spectral index β, $\Delta T_i(\nu) = \Delta T_{\mathrm{cmb},i} + \Delta T_{\mathrm{fore},i}\nu^\beta$, then given observations at two frequencies, one can solve for the CMB anisotropy component in terms of the unknown spectral index of the foreground,

$$\Delta T_{\mathrm{cmb},i} = \frac{\Delta T_i(\nu_1)\nu_1^{-\beta} - \Delta T_i(\nu_2)\nu_2^{-\beta}}{\alpha(\nu_1)\nu_1^{-\beta} - \alpha(\nu_2)\nu_2^{-\beta}}, \tag{2}$$

where $\alpha(\nu) = x^2 e^x/(e^x-1)^2$, with $x = h\nu/kT$, is the correction factor for the RJ approximation to a black body spectrum. As a check of our method we use this inferred CMB signal and perform a likelihood analysis. Here the total covariance matrix is composed of the CMB anisotropy flat bandpower theory covariance matrix, the instrumental noise matrix, and the (one-off diagonal) correlated noise (σ_n) found in the 31.7 GHz data (Leitch et al. 2000). This process assumes Gaussianity of the inferred CMB anisotropy signal[11] and the presence of only a single foreground. A constraint matrix to account for the removal of a constant offset is included in the analysis. After marginalizing over β and σ_n, the constraints on the level of CMB anisotropy agree with those found by Leitch et al. (2000). The constraints on β are not stringent with $\beta > -1.8$ ruled out at 2 σ. Although the data are unable to rule out a very steep spectrum foreground, based on correlating the data with Westerbork Northern Sky Survey (WENSS, Rengelink et al. 1997) 325 MHz maps, Leitch et al. (1997) conclude that the contribution of any $\beta < -2.2$ spectrum component is negligible. This then leaves a significant amount of foreground at 14.5 GHz of $\Delta T_{\mathrm{rms}} \sim 175$ μK, though it indicates that the 31.7 GHz data are almost entirely CMB anisotropy. A foreground signal as large as this does not show up for example in the Tenerife 15 GHz data. If this were representative of diffuse free-free emission the expected signal at larger scales would be enormous. Hence this foreground emission may be specific to the OVRO region.

The SP94 data were taken in two bands. The K_a band had four channels (centred at 27.25, 29.75, 32.25, and 34.75 GHz), hereafter K_a1, K_a2, K_a3, and K_a4, and the Q band had three (at 39.15, 41.45, and 43.75 GHz), hereafter $Q1$, $Q2$, and $Q3$. The beams had resolution of about 1° and there are 43 data points in each frequency channel, all at a declination of -62°, with RA ranging from 23° to 67°. The data were obtained using a sinusoidal $1.^\circ5$ chop with smooth, constant declination, constant velocity scans. See Gunderson et al. (1995) and Ganga et al. (1997) for more information on the SP94 experiment. Hamilton & Ganga (2001) have reported the detection of 100 μm-correlated emission at 1.6 σ confidence in the Q band data, resulting in a possible reduction of the deduced CMB anisotropy bandtemperature of Ganga et al. (1997). The K_a band data were found to be free of contamination from this template.

[11]While not yet tested on these angular scales, on slightly larger angular scales the CMB anisotropy appears to be Gaussian (Park et al. 2001a; Wu et al. 2001; Shandarin et al. 2001).

The IR dust and new high resolution H_α foreground emission templates we use are discussed in § 2. In § 3 we describe the correlation method. In § 4 we present results from correlating the OVRO data with the three maps of IR emission. Correlations of the H_α data with the OVRO data and the IR emission templates are discussed in § 5. In § 6 we study foregrounds in the SP94 data. § 7 consists of an overall discussion and conclusions.

2. The Foreground Templates

2.1. The Dust Maps

We use the 100 μm template (Schlegel et al. 1998) as a tracer of thermal dust emission and the 60 μm and 12 μm templates (D. Finkbeiner, private communication 2000) as tracers of emission from smaller dust grains. These templates are labelled i100, i60 and i12 in the tables that follow. To understand the difference in the structure of dust emission at the different frequencies, we studied the spectral index α (where intensity $I_\nu \propto \nu^\alpha$) of an assumed single component foreground emission between the frequencies of the three high frequency dust templates available. Emission in general decreases between 100 μm and 60 μm (that is the spectral index is negative over 90% of the sky). Between 60 μm and 12 μm the level of emission increases over 60% of the sky and the spectral index is positive for much of the high Galactic latitude region and in the rims of the cirrus. Over all, between 100 μm and 12 μm the emission seems to decrease though there is a kind of latitudinal dependence in the spectral index which is positive in some high-b regions.

To compare the spatial structure in these templates, we divided the sky into patches of a chosen size and found the correlation coefficient $\rho = \sum(y_i - \bar{y})(x_i - \bar{x})/\sqrt{[\sum(y_i - \bar{y})^2][\sum(x_i - \bar{x})^2]}$ between two dust templates (x and y) in these patches. The spatial structure in the 100 μm and 60 μm templates is found to be similar over most of the sky. The spatial structure in the 60 μm template is however quite different from that in the 12 μm template and the 12 μm template differs even more from the 100 μm template. The correlation between all templates in the OVRO fields is quite high, comparatively.

Minimum variance estimates of the correlation slope a (defined in § 3) of the OVRO data with different dust templates and with the dust column density template corresponding to the 100 μm emission (this is a template of the amount of thermal dust emission expected if the dust were all at a reference temperature of 18 K, Schlegel et al. 1998, and is labelled cdi100 in the tables) are discussed in § 4. Correlating the OVRO data with the column density template is necessary in order to make estimates comparable to those from the DMR data, as the temperature in the NCP region, and especially in the OVRO fields, is lower than the global average, resulting in lower dust emission and a correspondingly higher inferred correlation coefficient (this was emphasized by Finkbeiner & Schlegel 1999). Table 1 lists the dust temperatures and intensities in the OVRO fields, the whole of the NCP region (DEC $> 81°$), and the high Galactic latitude sky ($|b| > 30°$). Dust temperature has a range of 15 K to 23 K over the whole sky. Note that the temperature in

the OVRO fields is low enough to decrease the emission in these fields by a factor of 2.7, or dust emission in these fields would have been higher than is observed by this factor if dust here were at the high-b mean of 18 K. Note also that there is greater dust emission in the OVRO fields and this can play an important role in heating diffuse ionized gas.

2.2. H_α Observations

The H_α observations for the OVRO region were carried out on October 4, 2000 with the Virginia Tech Spectral Line Imaging Camera (SLIC) (Simonetti, Dennison, & Topasna 1996; Dennison, Topasna, & Simonetti 1997). The SLIC uses a 1.7 nm bandpass filter centered on H_α and a dual bandpass continuum filter with narrow passbands on either side of the H_α line. Both filters reject the [NII] lines at 654.8 and 658.3 nm. An $f/1.2$ Noct-Nikkor lens images a 5-degree radius circular field on a cyrogenically cooled TK 512×512 CCD camera. A separate auto-tracking CCD camera provides arcsecond precision tracking. The facility is located at a dark site at the Virginia Tech Horton Research Center.

We obtained seven 6-minute H_α images and six 3-minute continuum images approximately centered on the North Celestial Pole (NCP). We also recorded ten continuum flat field images using a flat field light box described in Simonetti et al. (1996). The images were combined and flat corrected in IRAF[12] using standard techniques (Dennison et al. 1997). For off-axis rays the bandpass of the interference filter shifts to longer wavelengths limiting the usable field to a 5-degree radius. The sensitivity to H_α is quite flat over this field, but was radially corrected using H_α observations of a flat H_α light box. H_α calibration was achieved through repeated observations of the bright planetary nebula M76, which we have previously determined to have an H_α flux of 7.95×10^{-11} ergs s^{-1} cm^{-2}.

The H_α image was then continuum-corrected through a weighted subtraction of the continuum image. This first required offsetting the continuum image by 1.93 pixels to achieve registration. (The different filters exhibit slightly different transverse gradients of optical thickness and thus displace the images by different amounts.) The H_α image was then smoothed by 0.5 pixel to match the resolution of the offset continuum image. The continuum-corrected image has significantly reduced stellar contamination, although the brightest stars are not well subtracted due to saturation effects.

The H_α line lies within a band of atmospheric OH emission, and because of the bandpass shift with incidence angle, our image contains contamination from the OH(6-1)$P_2(4)$ line at 656.9 nm in the center of the image and the OH(6-1)$P_1(3)$ line at 655.4 nm (Chamberlain 1961) in the outer part. The latter emission is manifested as a faint (≈ 3 R), diffuse ring with peak radius $\approx 4.^\circ6$. An

[12]IRAF is distributed by the National Optical Astronomy Observatory, which is operated by the Association of Universities for Research in Astronomy, Inc. under cooperative agreement with the National Science Foundation.

empirical model ring derived from azimuthally smoothed observations of a high-galactic-latitude field devoid of bright stars was used to remove the ring in the NCP field. The fit was optimized to remove the ring between 1.°6 and 3.°0, the region of interest in this study. Some contamination remains outside of this range. The bright star, Polaris, may also contribute to the contamination in the center of the image. A uniform gradient caused by scattered light as well as galactic starlight was also removed from the image. Because the image contains an unknown, nearly uniform background due to geocoronal H_α emission and scattered light, the median value of the final image was set equal to zero.

Coordinates were established using WCSTools (Mink 1997) which was used to fit to stars from the Hubble Guide Star Catalog. The final image is calibrated in rayleighs (R), where 1 R = $10^6/4\pi$ photons cm^{-2} s^{-1} sr^{-1}.

For the SP94 region the recently released SHASSA H_α (Gaustad et al. 2001) observations were used.

3. The Method

The method of cross-correlating microwave data with available foreground emission templates was used by Górski et al. (1996) and Banday et al. (1996) to simultaneously fit Galactic and extra-Galactic templates in Fourier space to the DMR data. The method has since been extended to real space and used by several others. It assumes that the microwave data consist of a superposition of CMB anisotropy, noise, and foreground emission components,

$$y = aX + x_{CMB} + n. \tag{3}$$

Here y is a data vector of N pixels, X is an $N \times M$ element matrix containing M foreground emission templates convolved with the experimental beam and processed by the observing strategy adopted, and a is a vector of size M that represents the levels at which these foreground templates are present in the data (each component of a is thus the correlation slope for the corresponding template). The vector n is the noise in the data and x_{CMB} is the CMB anisotropy convolved with the beam and processed by the observing strategy of the experiment. The noise and CMB are treated as mutually uncorrelated.

The minimum variance estimate of a, obtained by minimizing $\chi^2 = (y - aX)^T C^{-1} (y - aX)$, is

$$\hat{a} = [X^T C^{-1} X]^{-1} X^T C^{-1} y, \tag{4}$$

with errors $\Delta\hat{a}_i = \Sigma_{ii}^{1/2}$ where the matrix Σ is

$$\Sigma = < \hat{a}^2 > - < \hat{a} >^2 = [X^T C^{-1} X]^{-1}. \tag{5}$$

Here C is the total covariance matrix (the sum of the noise covariance matrix and the CMB covariance matrix). In these equations X and y are actually deviations of the corresponding quantities

from the weighted mean with weights given by C^{-1}. The rms amplitude of temperature fluctuations in the data that results from the correlation is $\Delta T = (\hat{a} \pm \delta\hat{a})\sigma_{\rm fore}$, where $\sigma_{\rm fore}$ is the rms deviation of the corresponding foreground template map.

Underlying this method of cross-correlating CMB data with maps of Galactic emission are the assumptions that the templates perfectly trace the spatial appearance of the respective components at the frequencies and angular scales of the CMB data, and that the templates are exhaustive, i.e., they are sufficient to explain all the structure in the data. In addition, for deriving the minimum variance estimator, we assume that the noise has zero mean and a Gaussian distribution.[13] With such caveats in mind, this method has been widely used to test for the presence of contaminants in CMB anisotropy data.

For OVRO the noise covariance matrix is diagonal. For SP94 the noise in a given pixel is correlated with noise in the same pixel in other channels of the same band. The noise in the K_a and Q bands are uncorrelated. The CMB anisotropy model covariance matrix causes non-trivial covariance between pixels of all channels. Hence we follow Hamilton & Ganga (2001) and present a values obtained for each channel when all channels are considered simultaneously. We also combine the a values for each template into a representative (average) number ($\bar{a}$) using both a spectral index n (here $\bar{a} = \bar{a_0}(\nu/\nu_0)^n$, where ν_0 is a reference frequency) of 0 and the best fit n, as described in Hamilton & Ganga (2001), for the K_a and Q bands separately and for both of them together. The best estimate of $\bar{a}$ is obtained, in the case $n = 0$, from

$$\bar{a} = \frac{\mathrm{Total}(\Sigma^{-1}\mathrm{a})}{\mathrm{Total}(\Sigma^{-1})} \tag{6}$$

where Total denotes the sum of all elements of a matrix or vector. This is thus a weighted average taking account of correlations between the a values of the different channels. The best fit n is obtained by minimizing, over a grid of values of n, $\chi^2 = (a - \bar{a_0}m)^T\Sigma^{-1}(a - \bar{a_0}m)$, where m is a vector with elements $m_i = (\nu_i/\nu_0)^n$.

4. Microwave-Dust Correlations in the OVRO Data

Table 2 lists results from correlating the two (14.5 and 31.7 GHz) OVRO data sets with each foreground template individually. Of the three templates of dust emission, the 100 μm template correlates best with the 14.5 GHz data, followed closely by the 60 μm template, and then the 12 μm template, all at a high level of significance. The reverse trend may be true for the 31.7 data, however the significance of dust correlation with the 31.7 GHz data is small. The correlation slope

[13] As noted in Mukherjee et al. (2001), violation of the assumptions that the templates are perfect and exhaustive can be expressed as an additional "missing" template which would by construction be perfectly compensating. If this template is uncorrelated with the templates used and has zero mean, we would expect only an increase in the noise level. If the template is correlated or has non-zero mean the estimate of the correlation slope a would be biased.

for the cdi100 template is a factor of about 3 lower than that for the i100 template. The 31.7 GHz results assume a correlated noise σ_n of 41 μK.[14] The χ^2 of the data by itself is 231 and 36.9 at 14.5 GHz and 31.7 GHz respectively (each data set has 36 independent observations, ignoring the small correlation between neighbouring pixels, and one parameter is being fit for so the number of independent degrees of freedom here is 35) for the flat-Λ model CMB anisotropy power spectrum we are using here[15]. These deductions are independent of the input power spectrum assumed, although significances of the correlations were marginally greater for open models.

We have tested for possible biases in this minimum variance analysis method by analyzing 1000 simulations of the data. These were made by simulating the CMB anisotropy component from a model and adding noise and a certain level of foreground on to it. We find that the weighted mean of the resulting correlation slopes turns out to be what was put in to a high degree of accuracy and the weighted rms deviation of the correlation slopes from the mean was in good agreement with the error bar for the chosen model. Thus not only is the method not biased, but the error bars are also accurate. Hence the high χ^2 at 14.5 GHz does indicate that the structure in the data has not been well accounted for by the templates, for if it were then the χ^2 per degree of freedom would have been near unity (see Table 2).

Figure 1 shows the 14.5 and 31.7 GHz OVRO data, and the structure in the dust templates in these fields after convolving with the OVRO beam and double differencing. Figure 1*c* shows that the level of CMB anisotropy inferred from eq. (2) is quite consistent with the 31.7 GHz data minus the 12 μm-correlated foreground, as also indicated by the χ^2 of the fit (see Table 2). The foreground at 14.5 GHz inferred from eq. (2) has an rms greater than that fitted using the 100 μm dust template fit (see Fig. 1*d*). However, the inferred foreground and the fitted foreground have similar spatial structure so it is possible that dust-correlated emission might satisfactorily explain the foreground in the 14.5 GHz OVRO data and the discrepancy might be due to uncertainties in the foreground template. If the templates are assumed to be close to perfect, then a better job can be done if we are able to cleanly separate the two components of emission likely to be present in the data, as discussed below. Another possibility is that there is an unaccounted-for foreground, possibly free-free emission uncorrelated with dust.

If the dust-correlated emission were entirely spinning dust emission, then a stronger correlation with the higher frequency dust templates should be expected, because these templates trace emission from small dust grains that are transiently heated to higher temperatures and emit (thermally at these high frequencies and rotationally at microwave frequencies) to get back to their ground state. That the 12 μm template is a clean tracer of emission from small dust grains and that such

[14]Leitch et al. (2000) argue that there is correlated noise of approximately $\sigma_n = 41$ μK present in the 31.7 GHz data. If we calculate the correlation slope after marginalizing over σ_n, the correlation slope so found is well within the error bars of the numerical values in Table 2 but with slightly larger error bars.

[15]The model was chosen from Ratra et al. (1997) and has matter density parameter $\Omega_0 = 0.4$, baryon density parameter $\Omega_B = 0.0125h^{-2}$, and $h = 0.6$ (where the Hubble constant $H_0 = 100h$ km s^{-1} Mpc^{-1}).

emission has a counterpart at microwave frequencies is still being tested, indirectly in work such as this and also more directly with the help of specialized observations (see, for example, Finkbeiner et al. 2001). Even if the 12 μm template is a clean tracer of the distribution of small dust grains, it may not be a good tracer of spinning dust emission which depends not only on the distribution of grains but on various other local factors. We proceed with these caveats in mind. The 100 μm template on the other hand is known to be dominated by emission from large dust grains which are in thermal equilibrium with the interstellar medium and radiate thermally at temperatures around 20 K. The distributions of small and large dust grains may be similar on large scales, but in some regions of the sky their small scale distribution could possibly differ (Weingartner and Draine 2000, small grains can remain locked in gas while larger grains can drift away). Thus, as noted by de Oliviera-Costa et al. (2001), shorter wavelength dust template maps might be expected to trace spinning dust at least as well as the 100 μm map and possibly better on small scales.

Table 3 lists results from correlating the OVRO data sets with two foreground templates jointly. When correlating jointly with the 12 μm and 100 μm templates, all the correlation in the 14.5 GHz data gets attributed to the 100 μm template. At 31.7 GHz there might be slight evidence of the emission getting attributed to the higher frequency template. As seen in Figure 1*b* and from the value of r in Table 3, the dust templates have similar spatial structure in the OVRO fields. When the 60 μm and 100 μm dust templates are correlated jointly with the OVRO data, the high correlation between these templates results in large uncertainty in separating the two dust emission components and so one cannot convincingly attribute the foreground emission to one template rather than the other. (When the 12 μm and 60 μm templates are jointly correlated the result is similar to when the 12 μm and 100 μm templates are jointly correlated.)

Thus, comparing the results of Table 2 and Table 3, the 12 μm-correlated emission is subdominant to the 100 μm-correlated emission in the 14.5 GHz OVRO data. If the 100 μm template is a tracer of free-free emission and the 12 μm template is a tracer of the distribution of small dust grains, then given that we find that these templates have similar spatial structure in the OVRO fields, if both emission components are present in the data, we would expect the above results if free-free emission dominates at 14.5 GHz and spinning dust emission dominates at 31.7 GHz.

Cleanly separating out the two components, that we expect are present in the data, at either frequency is difficult due to the presence of correlation between the dust templates. However, the 14.5 GHz data are consistent with about 92 ± 16 μK rms of spinning dust and hence, using the 100 μm-correlated emission results for the 14.5 GHz data (Table 2), with about 101 ± 22 μK rms of free-free emission at 14.5 GHz. This would translate into 19 ± 4 μK rms of free-free emission at 31.7 GHz.[16] The 100 μm template is able to pull out 18 ± 14 μK rms of correlated emission at 31.7 GHz (see Table 2), which is consistent with the level of free-free emission expected in the above scenario.

[16]The levels of free-free emission in the 14.5 GHz data and thereby in the 31.7 GHz data would be 121 ± 26 μK rms and 23 ± 5 μK rms respectively if we use the 100 μm-correlated emission results when correlating the data with the 12 μm and 100 μm templates jointly.

Note that the uncertainties in estimates of the correlation slope and the corresponding temperature fluctuations are comparable at the two frequencies. Hence, since the dust-correlated foreground components are present only at low levels at 31.7 GHz the significances of the correlations are low and become even lower when the data at this frequency are correlated with the 12 μm and 100 μm templates together. This then makes it hard to ascertain which component is dominant at 31.7 GHz. If we assume that the 12 μm-correlated component is dominant, then one is left with 16 ± 20 μK rms of spinning dust emission, which could thus be the dominant foreground emission component at 31.7 GHz.[17] The implied spinning dust spectral index between the two frequencies would then be $-2.2^{+1.2}_{-...}$, where the lower limit is undefined. This would explain why the spectral index of the 100 μm-correlated emission (Table 2) is steeper than expected for free-free, since the 100 μm-correlated emission at 14.5 GHz contains in it a spinning dust component as well. Correspondingly, the spectral index of the 12 μm-correlated emission (Table 2) is less steep than what might be expected for spinning dust based on the above estimate since the 12 μm-correlated emission at 31.7 GHz contains free-free emission as well. This exercise provides estimates of the levels of the two foreground emission components that are consistent with the data at the two OVRO frequencies. We next try to estimate the level of free-free emission that could be present in this data in the next section with the help of H_α data.

5. Deductions from H_α Data in the OVRO region

5.1. H_α Data and Microwave Emission

Since little is directly known about the amplitude and spatial distribution of free-free emission on the sky, the best way to trace it is through H_α emission. Given "clean" H_α observations, all that is needed to deduce the level of free-free emission is an estimate of the temperature of the ionized gas. The temperature of interstellar gas is about 10^4 K, estimated from measurements of line widths of emission from different mass ions and from intensities of collisionally excited forbidden lines (Haffner, Reynolds & Tufte 1999).

When the H_α data is convolved with the OVRO beam and double differenced, the data has an rms of 0.83 R in the OVRO fields. To find the visual extinction (which results from a combination of scattering and absorption) expected in the OVRO fields, we use the reddening maps provided by Schlegel et al. (1998) and find that the average reddening in the 36 OVRO fields is E(B-V) = 0.297 mag, implying a visual extinction of 0.921 mag (using R(V) = 3.1).[18] This implies that

[17]The uncertainty in this estimate is large because we have removed in quadrature the 100 μm-correlated component from the 12 μm-correlated emission. We note again that the experimental uncertainties in the estimates of dust correlated emission at 31.7 GHz are large, and this hampers our ability to identify and remove foregrounds from this data, even if these foregrounds are present at reasonable expected levels.

[18]The average extinction in the whole of the NCP (DEC $> 81^\circ$) region is 0.15 mag, in the $b > 30^\circ$ region it is 0.04

the H_α signal seen is at most $10^{-0.4\times0.921} = 0.428$ or 43% of the total H_α signal, or that the total H_α signal is 2.3 times that observed. This correction for extinction is not accurate as the decrease in the H_α surface brightness in a given direction depends not only on the total column density of dust but also on the unknown arrangement of the emitting and absorbing material along the line of sight (Reynolds & Haffner 2000 and the WHaM web page). In the high-b region in general extinction is small but in the OVRO fields it turns out to be quite large. Without attempting to make a more accurate correction for extinction, 0.83 R would imply an estimated H_α signal of 1.9 R and a free-free signal of 63 μK rms at 14.5 GHz. This level of free-free emission estimated from H_α data is an upper limit because some of the H_α signal could be due to incompletely subtracted stars. (But for these problems and extinction, the H_α signal should trace free-free emission.) If, in an attempt to remove stellar residuals, we set, prior to convolution and double differencing, the signal in pixels in the H_α map that show structure greater than 3σ to σ which is the local rms deviation from the local mean, where local here is taken to be from half a degree below to half a degree above the OVRO ring, then the rms of the resulting H_α signal in the 36 fields drops to 0.39 R (0.48 R before the double differencing).

Thus the upper limit on free-free emission inferred from H_α data is less than the free-free like dust-correlated signal found in § 4, and is much less than the signal in the OVRO data at 14.5 GHz that was found to have a spectral index like that of free-free emission (§ 1). Note that using their H_α observations, Simonetti et al. (1996) find, based on an rms H_α signal of 0.58 R, an rms free-free signal of 4.6 μK rms at 27.5 GHz on degree angular scales in the Saskatoon region of the NCP. Veeraraghavan & Davies (1997) have extensively cleaned the Gaustad, McCullough, & Van Buren (1996) H_α data and found rms fluctuations of 0.23 R in the NCP region (visual extinction in this region implies that this is $\sim$ 65% of the total H_α signal which therefore is $\sim$ 0.35 R). Their estimate is expected to be somewhat lower than ours because their data was subject to $6\farcm5$ median filtering followed by a $10'$ smoothing. Reynolds (1992) characterizes the high-b intensity distribution of diffuse H_α emission as 1.2 cosec$|b|$ R at large angular scales, whereas what is found at small angular scales is closer to 0.12 cosec$|b|$ R, so it seems that H_α intensity in general becomes considerably smoother on smaller angular scales. By comparison with the above estimates it might be true that the H_α signal in the OVRO fields is somewhat higher than the average though the need for correcting for extinction complicates such comparisons.

Dust temperature in the OVRO fields is high, by about 10%, compared to the average dust temperature in the high Galactic latitude region. High latitude dust is presumably heated by the same interstellar radiation as the WIM. Could there be a corresponding preferential heating of the WIM, given that gas gets heated more easily, such that the H_α data could be used to deduce a higher level of free-free emission in this region? For there to be 100 μK rms of free-free emission at 14.5 GHz, there needs to be about 3 R of (correlated) H_α fluctuations, or only 1.3 R in the presence of 43% visual extinction. If the gas temperature here were higher by a factor of 2.3, then the level

---

mag, and in the $b < -30^\circ$ region it is 0.05 mag.

of H_α fluctuations expected can come down to 0.83 R. The factor is 4.2 in order to comform to the level of 0.39 R.[19] Note that the power on the temperature in eq. (1) changes from 0.55 to 0.85 as the temperature crosses 2.6×10^4 K so that at high temperatures there is a greater contrast in the levels of free-free and H_α emission.

X-ray emission is also expected to be a good tracer of free-free emission (see, e.g., Smoot 1998) when the plasma is hot enough to produce X-rays via thermal bremsstrahlung. They both arise from the same mechanism but are at opposite extremes of the frequency spectrum. One can thus use X-ray observations to provide a temperature dependent upper limit for radio free-free emission.

The results of correlating the OVRO data with H_α templates of 0.89 and 0.39 R rms are given in Table 4. When correlating the H_α template with microwave data one may not find an observable correlation when there is significant visual extinction due to dust grains for which the H_α template has not been corrected so that the available template is not a good tracer of the spatial distribution of free-free emission, and also when the data contain a significant amount of another foreground. We see a pattern in Table 4. A significant negative correlation with the H_α template is found when the 14.5 GHz data are correlated jointly with the H_α and 100 μm or 12 μm templates with somewhat greater significance being attributed to the dust correlations than was obtained in the case of individual correlations (Table 2). From this we deduce that the structure in the H_α template partially traces the structure in the dust templates.

Correlating the data with H_α and rotated versions of the 12 μm template shows that the correlation seen is real and not just a chance occurrence.[20] Note however that this correlation appears only after the OVRO double differencing. Figures 2 and 3 show the structure in the H_α and dust emission templates in the OVRO fields before and after the double differencing respectively.

5.2. H_α Data and Infrared Emission

Diffuse hydrogen (present in ionized and neutral form) accounts for a significant fraction of interstellar matter and has a power input requirement equal to the supernovae output rate of our

[19]Leitch et al. (1997) conclude that the temperature needs to be higher by a factor ~ 100 in order to explain the level of foreground in the OVRO data. This is because they wanted to explain a free-free emission signal of 300 μK (a factor of 3 larger than what is argued for here), they had not taken the high visual extinction in the OVRO fields into account (this causes a difference of a factor of 2.3), and had an H_α signal of rms < 0.1 R (factor of 4 lower at least from what is found here), giving in total a difference of a factor of 28 from that found here, which when multiplied by 4.2 leads to the factor ~ 100.

[20]The real dust patch correlates with the highest correlation coefficient and has the most significant correlation slope with the H_α data, although 5% of the patches had greater values of the correlation slope. The real dust patch leads to the most significantly negatively correlated H_α signal jointly with a strong 12 μm-correlated signal in the OVRO data. Only one out of 60 dust patches correlated more significantly with the OVRO data, and this patch showed a less negative correlation with H_α data, with the dust and H_α signals barely correlated (according to both the correlation slope and correlation coefficient estimates).

Galaxy (Reynolds 1993). Ionized gas emits H_α and free-free in direct proportion, with the surface brightness of emission proportional to the electron density squared. It is important to note that these emissions only indirectly trace thermal emission from the dust associated with the ionized medium which has a surface brightness proportional to the density of dust. At low Galactic latitudes where dust opacity is considerable, dust absorbs H_α light and so about 25% of high latitude H_α emission is estimated to be scattered light (McCullough 1997). Lagache et al. (2000) have used H_α and HI data to decompose the far infrared thermal dust emission at high Galactic latitude into components associated with the WIM and the warm neutral medium (WNM). They confirm that about $20 - 30\%$ of thermal dust emission is associated with the WIM.

Further, the correlation between ionized gas and dust emission may be angular scale dependent, possibly increasing with increasing angular scale. McCullough (1997) argued for this when he found that the bulk of H_α emission on arcminute scales is not correlated with 100 μm emission but noted that Kogut et al. (1996b) concluded that on DMR angular scales at least a third and possibly the bulk of free-free emission comes from the component which correlates with dust emission. A simple model in which dust clouds have a lining which emits H_α or free-free emission has been used to explain this behavior with respect to angular scale. If external ionization by some mechanism (such as photoionization) creates a skin of ionized gas, then this model does predict that the degree of correlation between dust and ionized gas will be weak on scales smaller than the cloud size and strong on larger scales. Such an association has been revealed in some images (McCullough 1997; McCullough et al. 1999) while some observations indicate no association between H_α and X-ray/infrared/21-cm emissions (Haffner, Reynolds & Tufte 1998), so this needs to be investigated further.

When we calculate both the correlation coefficient as well as the correlation slope a between dust data at different frequencies and the H_α data, estimating the variance in these by correlating the H_α data with several controlled patches of dust emission, we do not find significant correlation with the dust templates in the OVRO fields. We find $a_{100\mu\mathrm{m},\,H_\alpha} = 0.1 \pm 0.3$ R(MJy/sr)$^{-1}$, $\rho_{100\mu\mathrm{m},\,H_\alpha} = 0.2 \pm 0.3$; $a_{60\mu\mathrm{m},\,H_\alpha} = 0.2 \pm 1.2$ R(MJy/sr)$^{-1}$, $\rho_{60\mu\mathrm{m},\,H_\alpha} = 0.1 \pm 0.3$; and $a_{12\mu\mathrm{m},\,H_\alpha} = 0 \pm 3.1$ R(MJy/sr)$^{-1}$, $\rho_{12\mu\mathrm{m},\,H_\alpha} = 0 \pm 0.2$. As noted earlier, low H_α-dust correlations may be acceptable due to various reasons, including the possibility that microwave-dust correlations are only in part due to free-free emission, in patches of the sky with high gas temperature and optical extinction, and on small angular scales.

After the OVRO double differencing the H_α signal correlates with the 12 μm dust template with a correlation slope of 5.4 ± 2.4 R(MJy/sr)$^{-1}$ and a correlation coefficient of 0.6 ± 0.2 in the OVRO fields. Sky rotations indicate that the H_α signal correlates best with the real 12 μm dust template, as discussed in the last section. The H_α signal does not correlate as significantly with the other dust templates even after the OVRO double differencing. However, we do not attach significance to the difference in the H_α correlations of the 100 and 12 μm maps[21] and deduce that

[21] From Figure 3, we see that the shape of the 12 μm signal is significantly different from that of the 100 μm signal

there appears to be some common structure in the H_α and dust templates after the OVRO double differencing. See Figures 2 and 3.

6. Foreground Emission in the UCSB South Pole 1994 Data

The correlations between the SP94 data and the dust templates are given in Table 5. The Haslam template does not show a positive correlation, and the 60 μm dust template is very much like the 100 μm template. So we present numbers here only for correlations with the 100 and 12 μm templates. The analysis is done ignoring the last 4 SP94 pixels that are close to and affected by a set of pixels at RA $\sim 69^\circ$ that have negative values of flux in the 12 μm map, apparently due to inaccurate source subtraction at that location.[22] We show the results of correlating the data with the 100 μm and the 12 μm templates individually because when the data are correlated with these templates jointly, then due to the high correlation between the templates, uncertainties increase further and nothing can be gained, given the already low level of contamination in this data. The numbers shown for each channel in Table 5 are derived by jointly correlating all channels of both SP94 bands. This is done because the CMB covariance matrix causes all channels to have cross-correlations. The data and the correlated emissions are shown in Figure 4. The results for the 100 μm case are similar to those presented in Hamilton & Ganga (2001). The 12 μm template is seen to also correlate somewhat with the data, particularly in the Q band.

The different a values for each SP94 band individually and both SP94 bands together can be combined using a spectral index of 0 or a best fit spectral index, as described in Hamilton & Ganga (2001) and in § 1. These results are listed in the Table 6. From this Table we see that the K_a band data does not correlate with the 100 μm template while the Q band data correlates marginally, the best fit spectral index when both bands are considered together is positive, and there is a greater than 2 σ detection of 100 μm-correlated emission, in agreement with Hamilton & Ganga (2001). Regarding 12 μm-correlated emission, we again find that the K_a band data does not correlate while the Q band data correlates marginally, the best fit spectral index when both bands are considered together is positive, and there is a greater than 2 σ detection of 12 μm-correlated emission when all channels are considered together with the best fit spectral index. The upper limit to the total

---

only in a few pixels after the differencing, for example between an RA of 14 and 15 hours where the slight dip in the 12 μm map seems to be due to an oversubtracted source, but the corresponding dip in the differenced H_α data is due partly to the presence of a large signal in the preceding pixel. These are unrelated causes.

[22]If we include all the SP94 pixels in the analysis, then we get a strong correlation of the SP94 data with the 12 μm template. The pixels in the 12 μm map that have negative flux values cause a dip in the signal in the last few pixels of the SP94 beam convolved template (even when the negative flux values are set to 0 or to a value lower than the local mean, assuming that we can not really know the level of diffuse emission here due to the presence of a source that has not been accurately removed). There is a similar dip in the microwave signal in the different channels of the SP94 data (see Figure 4 of Ganga et al. 1997 and Figure 2 of Hamilton & Ganga 2001), and this results in a strong correlation with the 12 μm template.

contamination from dust templates in the SP94 data is $\Delta T_{\rm rms} = 26 \pm 11$ μK when the results of all channels are combined using estimates of the best fit spectral indices. This is an upper limit because the 100 and the 12 μm correlated emission have been coadded, even though these templates are seen to have very similar structure. We are unable to say from this kind of a correlation analysis which of these two components is dominant or even whether these correlations are due to physically distinct components. We expect, from observations of far-infrared and mid-infrared emissions, that the dust grains that emit at 100 μm are physically distinct from the dust grains that emit at 12 μm. The two kinds of dust grains however may be well mixed, making it difficult to separate any microwave components associated with them using template correlations. Proof of the 12 μm-correlated emission being distinct from the 100 μm-correlated emission in microwave data must then be found with the help of observations that verify the spinning dust model, or another similar model, in detail (see discussion in § 7). Most of the contamination is in the Q band of the SP94 data ($\Delta T_{\rm rms} = 32 \pm 21$ μK is the total dust-correlated emission in this band), while no evidence is found for the contamination of K_a band data. This is in agreement with the conclusions of Ganga et al. (1997); also see Ratra et al. (1999b).

Sky-rotations (correlating the data with template dust maps obtained by rotating the initial map around the Galactic poles and by inverting the North and South Poles) indicate that the correlations are about as significant as the numbers indicate. In other words the correlation that could arise from a random alignment between CMB anisotropies and the dust template has been taken into account in the analysis by the data and CMB covariance matrices, and the rms of the correlations from random patches agrees well with the error bars obtained by the correlation method. Correlations similar to those obtained using the 100 μm template are obtained when the data are correlated with the column density template for 100 μm emission, indicating that the dust temperature in the SP94 pixels is not radically different from the average.

We analyze the structure of H_α signal in the SP94 pixels using data from SHASSA. These data are available at a resolution of $0.^\circ1$. No significant correlation is found when the SP94 data are correlated with the SP94 beam convolved H_α data. When the SP94 data are correlated jointly with the 100 μm and H_α templates, a negative correlation is attributed to the H_α template while a positive correlation is attributed to the 100 μm template (see Table 7). The positive correlation is more significant than that obtained when the SP94 data were correlated with this dust template individually (compare Tables 5 and 7). This is illustrated in Figure 5 and indicates that the H_α template and the dust template have common structure. When the SP94 data are correlated jointly with the 12 μm and the H_α templates, then the results are nearly the same as in the case of individual correlations with these templates, implying that these two templates do not have much common structure. Thus, like in the OVRO case, we find that the structure in the H_α template has something in common with structure of dust emission, and that in such a situation the correlation method is unable to separate the H_α-correlated signal and the rest of the dust-correlated signal.

The correlation slope between the H_α signal and the 100 μm dust emission, for example for channel $Q1$, is 0.3 ± 0.2 R(MJy/sr)$^{-1}$ (10% of the rotated dust patches have greater correlation

slope, the significance of the correlation slope with the real dust patch is 7.7σ, 8% of the dust patches correlated with greater significance, and the rms of the significances was 4.4σ). The correlation coefficient is 0.4 ± 0.2 (the same 8% of the dust patches had greater correlation coefficient than the real dust patch). Here the variance is found by correlating the H_α data with 144 rotated versions of the dust emission template. As in the case of OVRO, the H_α and dust data correlate better after the chopping strategy of the SP94 experiment has been simulated on these data.

As a consequence of foreground contamination the deduced SP94 bandtemperature (Ganga et al. 1997) in the Q band could go down in amplitude by at most 21% , to 41 ± 26 μK. Although the dust correlations in this data set are not very significant, the SP94 data does not contradict the hypothesis that there are two components of dust correlated emission present in the data, at comparable levels at these frequencies and angular scales. Other CMB data sets need to be studied to confirm this.

7. Discussion and Conclusion

Dust-correlated emission seems to consist of free-free emission as well as another component. The amplitude of dust-correlated emission in DMR data at 53 GHz is $\Delta T_{\rm rms} = 7.1 \pm 1.7$ μK, while the total amount of free-free emission is $\Delta T_{\rm rms} = 5.2 \pm 4.2$ μK using multifrequency data (Kogut et al. 1996b). Since at that time no other dust-correlated component of emission was expected to be found at these frequencies, it was concluded that the correlated component forms at least a third (at 95% confidence) of the total free-free emission and possibly even the bulk of it. If instead free-free emission were only a part of the total dust-correlated emission (with the 12 μm and 100 μm templates being similar in structure at large angular scales) then the remaining part is constrained to be 5 ± 4 μK rms at 53 GHz on DMR scales. The 5 ± 4 μK rms of free-free emission at 53 GHz translates to 76 ± 61 μK rms of emission at 14.5 GHz and further to 26 ± 20 μK rms at OVRO scales using the power spectrum for free-free emission estimated by Veeraraghavan & Davies (1997), $C_l \propto l^{-2.3}$ (they estimated the power spectrum directly from cleaned and destriped H_α maps and so may have obtained a more reliable estimate of the free-free emission power spectrum than did Kogut et al. 1996a). This implies free-free emission of < 66 μK rms at 95% confidence, consistent with the rough upper limits indicated by H_α observations. If we remove this amount from the OVRO total 100 μm-correlated emission at 14.5 GHz we are left with emission of amplitude roughly consistent with that of 12 μm-correlated emission, $\Delta T_{\rm rms} = 92 \pm 16$ μK. If this component is independent of angular scale, then these estimates together with the amplitude at 53 GHz imply a spectral index $\beta = -2.2^{+0.6}_{-1.4}$ for the 12 μm-correlated component.

Similarly if the free-free emission at 53 GHz is this time extrapolated to 36 GHz, the implied signal is $\Delta T_{\rm rms} = 11 \pm 9$ μK, and this implies $\Delta T_{\rm rms} = 6 \pm 5$ μK on SP94 scales, indicating a 95% upper limit of 16 μK rms. From a combination of data from all SP94 channels, the estimated level of 100 μm-correlated emission is $\Delta T_{\rm rms} = 21 \pm 9$ μK (for $n = 2.2$, with $a = 54 \pm 23$ μK(MJy/sr)$^{-1}$) at 36 GHz. The contamination in this case is restricted to the Q band channels, and using the

Q band channels only, the amplitude of 100 μm-correlated emission is $\Delta T_{\rm rms} = 24 \pm 16$ μK (for n=0.8, with $a = 63 \pm 42$ μK(MJy/sr)$^{-1}$) at 42 GHz. Thus these estimates are consistent. Note that, from Fabry-Perot interferometer observations of H_α emission in this region, Marcelin et al. (1999) estimate a maximum free-free temperature anisotropy of less that 10 μK rms at 30 GHz (K_a-band). We find that the 12 μm-correlated emission in the SP94 data is 16 ± 7 μK rms at 36 GHz, if one correlates the data with this template individually. The two dust templates are similar in the SP94 pixels (as in the OVRO pixels) and we are not able to distinguish between or separate out the two components or determine which of these dominates. If it is true that the 100 μm template correlations are only in part free-free, the remaining being another component that the 12 μm template traces better, then the SP94 data does not contradict this but rather fits in well. The implied spectral index for the 12 μm-correlated component, given its rough amplitude at 53 GHz, is $\beta = -3.0^{+3.0}_{-5.1}$, if this component is independent of angular scale, with the uncertainty here being large mainly due to the large uncertainty in the estimated level of such emission at 53 GHz. These spectral index estimates may be consistent with the spinning dust hypothesis, becoming more negative between 36 and 53 GHz, that is at higher frequencies. This hypothesis also explains why Veeraraghavan & Davies (1997) obtain a considerably lower normalization for the free-free emission power spectrum derived from H_α maps than did Kogut et al. (1996a), who used dust-correlated microwave emission (which is only in part free-free emission). It also explains the flatter spectrum of free-free emission given that the remaining dust-correlated emission makes a contribution to temperature fluctuations that seems to be independent of angular scale, from the estimates available to date.

Figure 6 is a plot of 12 μm-correlated emission in the OVRO and SP94 microwave emission data. Spinning dust emission might have been detected in microwave data with significant levels of emission at about 15 GHz. There is, however, free-free emission present as well, and separating the two components continues to be difficult. The evidence for the presence of these two components of foreground emission in these microwave data sets is not conclusive. We need to check, for example, whether the correlation slope between the 12 μm template and DMR 53 GHz data lies on the spectral curve shown. In order to correlate the DMR data with the 12 μm template we may need to await the cleaning of the template as the signal at 12 μm is contaminated significantly by zodiacal emission. Modelling zodiacal emission is a complex task and this could take some time. We were able use the 12 μm template in its present state as we consider only small regions of the sky, and in these few pixels far from the ecliptic plane there does not seem to be obvious contamination. When a similar analysis is done using the newest Tenerife data (de Oliviera-Costa et al. 2001, Macias-Perez et al., in preparation), it is found, as before (Mukherjee et al. 2001), that the high Galactic latitude region ($b > 30^\circ$) is not significantly contaminated, but in the region $20^\circ < b < 30^\circ$ the 15 GHz data shows dust-correlated contamination, and about half of the 100 μm-correlated emission here is correlated with the 12 μm template. This supports the idea that both free-free and spinning dust emission are probably present at comparable levels at this frequency, although there are regions in the high Galactic latitude sky that are less contaminated. Tenerife data, covering a large region of the sky, requires a more detailed analysis before reliable numbers can be estimated

because, as mentioned here and described in Mukherjee et al. (2001), only some regions of the sky show correlated emission, and data from declinations separated by $2.^\circ5$ on the sky have different levels of contamination. Whether the 12 μm-correlated emission in other CMB anisotropy data sets follow the spectral pattern of Figure 6 remains to be determined. Higher quality data from the newer CMB experiments, such as CBI and DASI, and that anticipated from MAP, should help resolve this issue.

Rather than having to use thermal dust emission as an indirect tracer of free-free emission, data from new H_α observations should soon provide a template that more directly traces free-free emission. However, converting the H_α data into a reliable template of free-free emission is challenging in itself, due to complications such as varying levels of extinction and temperature of ionized gas. A careful comparison of structures in a high resolution H_α map, with information on extinction and gas temperatures, to structures in microwave and IR data is needed. X-ray and ultraviolet observations can help place constraints on gas temperature. The spinning dust hypothesis itself can be studied by making pointed observations towards dust features predicted to emit significant amounts of spinning dust emission (Finkbeiner et al. 2001). Such observations can more easily and significantly constrain the spinning dust model. Even if these foreground contaminants are present only at low levels in CMB anisotropy data, it is important that they be understood and removed to high precision, especially if one wishes to study higher order statistics and non-Gaussian signatures in the CMB anisotropy data (see, e.g., Park et al. 1998; Coles & Chiang 2000; Barreiro & Hobson 2001; Park, Park, & Ratra 2001b).

In summary, we discuss a scenario in which dust correlated microwave emission in the OVRO and SP94 microwave anisotropy data sets consists of free-free emission as well as another component. This is motivated by the facts that free-free emission by itself is not expected to result in strong microwave-IR correlations and that free-free emission is constrained by H_α emission in both the data sets to be much less that the amplitude of dust-correlated emission. The H_α data and dust emission data seem to have some common structure, but dust emission correlates better with microwave data. If we use the power spectrum of Veeraraghavan & Davies (1997) for free-free emission and assume that the other component is independent of angular scale, as observations to date seem to roughly indicate, then we find that from spectral index considerations the other component could be spinning dust emission. Other CMB data sets would have to be studied to confirm this. Given that the two components have different power spectra, which component dominates in a given data set would depend on both the frequency as well as the relevant angular scales. Higher quality CMB anisotropy data, more knowledge about the characteristics of dust emission at high frequencies and at microwave frequencies, and high resolution H_α data over large portions of the sky, will all be valuable in obtaining a clearer picture of foreground contaminants in low frequency microwave data.

We are indebted to D. Finkbeiner for valuable and detailed comments on the manuscript. We acknowledge useful discussions with R. Kneissl, J. Macias-Perez, R. Reynolds, and T. Souradeep, and the use of the WCS Tools software (Mink 1997). We thank D. Finkbeiner for the 12 μm dust

template, J. Gaustad and P. McCullough for the SHASSA H_α data (SHASSA was produced with support from the NSF), and D. Mink for assistance with coordinate fitting in the VTSS H_α observations, near a singularity in the celestial coordinate system. BD and JHS acknowledge support from NSF grants AST-9800476 and AST-0098487 and a Horton Foundation grant to Virginia Tech. The Miles C. Horton, Sr. Research Center is operated by the Virginia Polytechnic Institute and State University with support from the Horton Foundation. This work was partially carried out at the Infrared Processing and Analysis Center and the Jet Propulsion Laboratory of the California Institute of Technology, under a contract with the National Aeronautics and Space Administration. PM and BR acknowledge support from NSF CAREER grant AST-9875031.

Table 1. Dust Temperatures and 100 μm Template Intensities

Region	Average Dust Temperature (K)	$I_{\rm i100}$[a](MJy/sr)	$I_{\rm cdi100}$[b](MJy/sr)
OVRO Fields	16.2	5.90	16.1
NCP (DEC $> 81°$)	16.9	4.08	8.41
$\|b\| > 30°$	17.9	2.12	2.56

[a]Intensity of the 100 μm dust emission template.

[b]Intensity of the 100 μm column density template that assumes a constant dust temperature of 18 K.

Table 2. Results of Correlating the OVRO Data with Each Dust Template

	14.5 GHz				31.7 GHz				
Template	$a \pm \delta a$[a]	$\frac{a}{\delta a}$	ΔT (μK)	χ^2	$a \pm \delta a$[a]	$\frac{a}{\delta a}$	ΔT (μK)	χ^2	β
cdi100[b]	50.8 ± 5.3	9.6	134 ± 14.0	139	6.6 ± 5.3	1.2	17.3 ± 14.0	35.4	$-2.6^{+0.9}_{-2.2}$
i100[c]	145 ± 15.7	9.2	136 ± 14.8	146	19.5 ± 15.2	1.3	18.3 ± 14.3	35.3	$-2.6^{+0.9}_{-2.0}$
i60[d]	1210 ± 133	9.1	138 ± 15.1	148	191 ± 128	1.5	21.7 ± 14.6	34.7	$-2.4^{+0.8}_{-1.5}$
i12[e]	2190 ± 373	5.9	91.6 ± 15.6	196	578 ± 361	1.6	24.1 ± 15.1	34.4	$-1.7^{+0.9}_{-1.5}$

[a]Correlation slope a in units of μK(MJy/sr)$^{-1}$.

[b]The 100 μm column density template that assumes a constant dust temperature of 18 K.

[c]The 100 μm dust emission template.

[d]The 60 μm dust emission template.

[e]The 12 μm dust emission template.

Table 3. Results from Correlating the OVRO Data with Two Dust Templates

	14.5 GHz				31.7 GHz				
Template	$a \pm \delta a$ [a]	$\frac{a}{\delta a}$	ΔT (μK)	χ^2	$a \pm \delta a$ [a]	$\frac{a}{\delta a}$	ΔT (μK)	χ^2	r [b]
i12	-246 ± 506	-0.5	-10.0 ± 20.6	146	484 ± 480	1.0	20.2 ± 20.1	34.3	0.67
i100	152 ± 21.3	7.1	143 ± 20.1		6.0 ± 20.3	0.3	5.6 ± 19.1		
i12	-534 ± 539	-1.0	-21.7 ± 21.9	147	396 ± 505	0.8	16.1 ± 20.5	34.1	0.72
i60	1350 ± 193	7.0	153 ± 21.9		92.3 ± 179	0.5	10.5 ± 20.4		
i60	531 ± 336	1.6	60.5 ± 38.2	143	245 ± 312	0.8	27.9 ± 35.5	34.7	0.92
i100	87.3 ± 39.6	2.2	82.1 ± 37.3		-7.1 ± 37.1	-0.2	-6.7 ± 34.9		

[a]Correlation slope a in units of μK(MJy/sr)$^{-1}$.

[b]$r = \Sigma_{ij}^{-1}/(\Sigma_{ii}^{-1}\Sigma_{jj}^{-1})^{0.5}$ is the weighted correlation coefficient between the two templates, indexed i and j here.

Table 4. Results from Correlating the OVRO Data with the H_α Template and with H_α and Dust Templates Jointly[a]

	14.5 GHz				31.7 GHz					
	$a \pm \delta a$[b]	$\frac{a}{\delta a}$	ΔT (μK)	χ^2	$a \pm \delta a$[b]	$\frac{a}{\delta a}$	ΔT (μK)	χ^2	r[c]	ρ[d]
H_α	-17.0 ± 19.6	-0.9	-15.7 ± 18.0	230	-2.0 ± 17.9	-0.1	-1.7 ± 14.8	36.9		
H_α	-36.0 ± 19.7	-1.8	-29.9 ± 16.4	142	-5.3 ± 18.0	-0.3	-4.4 ± 15.0	35.2	0.1	0.1
i100	148 ± 15.8	9.4	139 ± 14.9		20.1 ± 15.4	1.3	18.9 ± 14.5			
H_α	-70.5 ± 21.1	-3.3	-58.7 ± 17.6	185	-18.6 ± 20.0	-0.9	-15.5 ± 16.6	33.5	0.4	0.5
i12	2700 ± 403	6.7	110 ± 16.3		747 ± 404	1.8	30.3 ± 16.4			
H_α	-65.3 ± 40.8	-1.6	-25.6 ± 16.0	228	-19.8 ± 37.3	-0.5	-7.8 ± 14.6	36.6		
H_α	-122 ± 41.3	-2.9	-47.8 ± 16.2	137	-29.0 ± 37.9	-0.8	-11.4 ± 14.9	34.7	0.1	0.2
i100	152 ± 15.9	9.5	143 ± 14.9		21.5 ± 15.5	1.4	20.3 ± 14.6			
H_α	-211 ± 45.4	-4.6	-82.9 ± 17.8	175	-70.7 ± 43.9	-1.6	-27.7 ± 17.2	31.8	0.4	0.6
i12	3040 ± 415	7.3	123 ± 16.8		936 ± 424	2.2	38.0 ± 17.2			

[a]The upper half of the Table uses the 0.83 R rms H_α template and the lower half uses the 0.39 R rms H_α template.

[b]Correlation slope a in units of μK/R.

[c]Covariance matrix weighted correlation coefficient.

[d]Unweighted correlation coefficient.

Table 5. Results from Correlating Data from all SP94 Channels (39 of 43 pixels only) with the 100 μm and 12 μm Dust Templates Individually

Template	Channel	$a \pm \delta a$ (μK(MJy/sr)$^{-1}$)	$\frac{a}{\delta a}$	ΔT (μK)
i100	K_a1	1.5 ± 39.2	0.0	0.5 ± 13.6
	K_a2	46.6 ± 40.4	1.1	16.5 ± 14.3
	K_a3	15.1 ± 41.6	0.4	5.4 ± 15.0
	K_a4	67.0 ± 42.7	1.6	24.4 ± 15.6
	$Q1$	59.0 ± 47.3	1.2	22.0 ± 17.6
	$Q2$	71.2 ± 44.6	1.6	26.8 ± 16.8
	$Q3$	67.5 ± 45.3	1.5	25.6 ± 17.2
i12	K_a1	-126 ± 849	-0.1	-2.0 ± 13.3
	K_a2	683 ± 864	0.8	11.1 ± 14.1
	K_a3	-39.1 ± 880	0.0	-0.7 ± 14.7
	K_a4	999 ± 894	1.1	17.2 ± 15.4
	$Q1$	1030 ± 974	1.1	18.3 ± 17.3
	$Q2$	1020 ± 914	1.1	18.4 ± 16.5
	$Q3$	1370 ± 925	1.5	25.1 ± 17.0

Table 6. Results from Combining Channels of the SP94 Data[a]

	K_a				Q				$K_a + Q$			
Template	n	$a \pm \delta a$[b]	$\frac{a}{\delta a}$	ΔT[c]	n	$a \pm \delta a$[b]	$\frac{a}{\delta a}$	ΔT[c]	n	$a \pm \delta a$[b]	$\frac{a}{\delta a}$	ΔT[c]
i100	0.0	28.9 ± 32.3	0.9	8.5 ± 11.3	0.0	62.6 ± 42.7	1.5	23.4 ± 16.1	0.0	24.8 ± 34.4	0.7	5.0 ± 12.1
	[d] ...	...	...	...	0.8	63.1 ± 42.3	1.5	23.9 ± 16.0	2.2	53.4 ± 22.8	2.3	20.8 ± 8.9
i12	0.0	129 ± 716	0.2	-0.2 ± 11.5	0.0	1150 ± 799	1.4	20.1 ± 14.4	0.0	431 ± 756	0.6	0.7 ± 12.2
	[d] ...	...	...	...	3.2	1190 ± 697	1.7	22.1 ± 12.9	3.0	854 ± 359	2.4	16.2 ± 6.8

[a]We combine the K_a band channels, the Q band channels, and finally all the channels, using first a spectral index $n = 0$ and then the best fit n for the case when the SP94 data are correlated with the 100 μm and 12 μm templates individually. Here K_a band results use a reference frequency $\nu_0 = 30$ GHz, Q band results use $\nu_0 = 42$ GHz, and when all channels are combined together results are given for $\nu_0 = 36$ GHz. Only 39 of 43 pixels for each channel were considered in this analysis.

[b]Correlation slope a in units of μK(MJy/sr)$^{-1}$.

[c]Temperature anisotropy ΔT in units of μK.

[d]In this case the best fit n was greater than 15, outside the range of the n grid used.

Table 7. Results from Correlating Data from all SP94 Channels (39 of 43 pixels only) with the H_α data and the 100 μm Dust Templates Jointly ($r = 0.4$)

Template	Channel	$a \pm \delta a$[a]	$\frac{a}{\delta a}$	ΔT (μK)
H_α	K_a1	0.1 ± 6.3	0.0	0.1 ± 12.8
	K_a2	-3.0 ± 6.0	-0.5	-6.8 ± 13.6
	K_a3	0.5 ± 5.9	0.1	1.2 ± 14.4
	K_a4	-6.3 ± 5.8	-1.1	-16.3 ± 15.1
	$Q1$	-4.6 ± 6.2	-0.7	-13.1 ± 17.5
	$Q2$	-3.7 ± 5.7	-0.6	-10.7 ± 16.5
	$Q3$	-6.8 ± 5.7	-1.2	-20.2 ± 17.1
i100	K_a1	7.5 ± 45.4	0.2	2.6 ± 15.7
	K_a2	62.2 ± 46.4	1.3	22.0 ± 16.4
	K_a3	19.9 ± 47.6	0.4	7.2 ± 17.1
	K_a4	93.8 ± 48.6	1.9	34.2 ± 17.7
	$Q1$	80.7 ± 53.3	1.5	30.1 ± 19.9
	$Q2$	89.6 ± 50.3	1.8	33.7 ± 18.9
	$Q3$	96.6 ± 51.1	1.9	36.7 ± 19.4

[a]Correlation slope a in units of μK/dR for the H_α template, where 1 dR=0.1 R, and in units of μK(MJy/sr)$^{-1}$ for the 100 μm template

REFERENCES

[1]Banday, A.J., Górski, K.M., Bennett, C.L., Hinshaw, G., Kogut, A., & Smoot, G.F. 1996, ApJ, 468, L85

[2]Barreiro, R.B., & Hobson, M. 2001, MNRAS, 327, 813

[3]Bartlett, J.G., & Amram, P. 1998, astro-ph/9804330

[Chamberlain 1961]Chamberlain, J.W. 1961, Physics of the Airglow and Aurora (New York: Academic)

[4]Coble, K., et al. 1999, ApJ, 519, L5

[5]Coles, P., & Chiang, L.Y. 2000, Mining the Sky, ed. A.J. Banday et al. (Berlin: Springer-Verlag), in press (astro-ph/0010521)

[6]Dennison, B., Topasna, G.A., & Simonetti, J.H. 1997, ApJ, 474, L31

[7]de Oliviera-Costa, A., et al. 1997, ApJ, 482, L17

[8]de Oliviera-Costa, A., et al. 2000, ApJ, 542, L5

[9]de Oliviera-Costa, A., et al. 2001, astro-ph/0010527

[10]de Oliviera-Costa, A., Tegmark, M., Gutierrez, C.M., Jones, A.W., Davies, R.D., Lasenby, A.N., Rebolo, R. & Watson, R.A. 1999, ApJ, 527, L9

[11]de Oliviera-Costa, A., Tegmark, M., Page, L.A, & Boughn, S.P. 1998, ApJ, 509, L9

[12]Draine, B.T., & Lazarian, A. 1998a, ApJ, 494, L19

[13]Draine, B.T., & Lazarian, A. 1998b, ApJ, 508, 157

[14]Draine, B.T., & Lazarian, A. 1999, in ASP Conf. Ser. 181, Microwave Foregrounds, ed. A. de Oliveira-Costa & M. Tegmark (San Francisco: ASP), 133

[15]Ferrara, A., & Dettmar, R.-J. 1994, ApJ, 427, 155

[16]Finkbeiner, D.P., & Schlegel, D.J. 1999, in ASP Conf. Ser. 181, Microwave Foregrounds, ed. A. de Oliveira-Costa & M. Tegmark (San Francisco: ASP), 101

[17]Finkbeiner, D.P., Schlegel, D.J., Frank, C. & Heiles, C. 2001, ApJ, in press, astro-ph/0109534

[18]Ganga, K., Ratra, B., Gunderson, J.O., & Sugiyama, N. 1997, ApJ, 484, 7

[19]Ganga, K., Ratra, B., Lim, M.A., Sugiyama, N., & Tanaka, S.T. 1998, ApJS, 114, 165

[20]Gaustad, J.E., McCullough, P.R., Rosing, W., & Van Buren, D. 2001, PASP, 113, in press

[21]Gaustad, J.E., McCullough, P.R., & Van Buren, D. 1996, PASP, 108, 351

[22]Górski, K.M., Banday, A.J., Bennett, C.L., Hinshaw, G., Kogut, A., Smoot, G.F., & Wright, E.L. 1996, ApJ, 464, L11

[23]Gunderson, J.O., et al. 1995, ApJ, 443, L57

[24]Haffner, L.M., Reynolds, R.J., & Tufte S.L. 1998, ApJ, 501, L83

[25]Haffner, L.M., Reynolds, R.J., & Tufte S.L. 1999, ApJ, 523, 223

[26]Hamilton, J.-Ch., & Ganga K.M. 2001, A&A, 368, 760

[27]Haslam, C.G.T., Klein, U., Salter, C.J., Stoffel, H., Wilson, W.E., Cleary, M.N., Cooke, D.J., & Thomasson, P. 1981, A&A, 100, 209

[28]Jonas, J.L., Baart, E.E., & Nicolson, G.D. 1998, MNRAS, 297, 977

[29]Knox, L., & Page, L. 2000, Phys. Rev. Lett., 85, 1366

[30]Kogut, A. 1997, AJ, 114, 3

[31]Kogut, A. 1999, in ASP Conf. Ser. 181, Microwave Foregrounds, ed. A. de Oliveira-Costa & M. Tegmark (San Francisco: ASP), 91

[32]Kogut, A., Banday, A.J., Bennet, C.L., Górski, K.M., Hinshaw, G. & Reach, W.T. 1996a, ApJ, 460, 1

[33]Kogut, A., Banday, A.J., Bennet, C.L., Górski, K.M., Hinshaw, G., Smoot, G.F. & Wright, E.L. 1996b, ApJ, 464, L5

[34]Lagache, G., Haffner, L.M., Reynolds, R.J., & Tufte S.L. 2000, A&A, 354, 247

[35]Lawson, K.D., Mayer, C.J., Osborne, J.L. & Parkinson, M.L. 1987, MNRAS, 225, 307

[36]Leitch, E.M., Readhead, A.C.S., Pearson, T.J., & Myers, S.T. 1997, ApJ, 486, L23

[37]Leitch, E.M., Readhead, A.C.S., Pearson, T.J., Myers, S.T., Gulkis, S., & Lawrence C.R. 2000, ApJ, 532, 37

[38]Lim, M.A., et al. 1996, ApJ, 469, L69

[39]Marcelin, M., Amram, P., Bartlett, J.G., Valls-Gabaud, D., & Blanchard A. 1999, A&A, 338, 1

[40]McCullough, P.R. 1997, ApJ, 113, 6

[41]McCullough, P.R., Gaustad, J.E., Rosing, W., & Van Buren, D. 1999, astro-ph/9902248

[42]Mink, D.J. 1997, in ASP Conf. Ser. 125, Astronomical Data Analysis Software and Systems VI, ed. G. Hunt and H. E. Payne (San Francisco: ASP), 249

[43]Mukherjee, P., Jones, A.W., Kneissl, R., & Lasenby, A.N. 2001, MNRAS, 320, 224

[44]Netterfield, C.B., et al. 2001, ApJ, submitted (astro-ph/0104460)

[45]Park, C., Colley, W.N., Gott, J.R., Ratra, B., Spergel, D.N., & Sugiyama, N. 1998, ApJ, 506, 473

[46]Park, C.-G., Park, C., & Ratra, B. 2001b, astro-ph/0107004

[47]Park, C.-G., Park, C., Ratra, B., & Tegmark, M. 2001a, ApJ, 556, 582

[48]Podariu, S., Souradeep, T., Gott, J.R., Ratra, B., & Vogeley, M.S. 2001, ApJ, 559, 9

[49]Pryke, C., Halverson, N.W., Leitch, E.M., Kovac, J., Carlstrom, J.E., Holzapfel, W.L., & Dragovan, M. 2001, ApJ, submitted (astro-ph/0104490)

[50]Ratra, B., Ganga, K., Stompor, R., Sugiyama, N., de Bernardis, P., & Górski, K.M. 1999a, ApJ, 510, 11

[51]Ratra, B., Stompor, R., Ganga, K., Rocha, G., Sugiyama, N., & Górski, K.M. 1999b, ApJ, 517, 549

[52]Ratra, B., Sugiyama, N., Banday, A.J., & Górski, K.M. 1997, ApJ, 481, 22

[53]Reich, P., & Reich, W. 1986, A&AS, 63, 205

[54]Rengelink, R.B., Tang, Y., Debruyn, A.G., Miley, G.K., Bremer, M.N., Rottgering, H.J.A., & Bremer, M.A.R. 1997, A&AS, 124, 259

[55]Reynolds, R.J. 1992, ApJ, 392, L35

[56]Reynolds, R.J. 1993, in AIP Proceedings 278, ed. S.S. Holt & F. Verter (New York: AIP), 156

[57]Reynolds, R.J., & Haffner, L.M. 2000, PASP, in press (astro-ph/0010618)

[58]Reynolds, R.J., Tufte, S.L., Kung, D.T., McCullough, P.R., & Heiles, C. 1995, ApJ, 448, 715

[59]Rocha, G., Stompor, R., Ganga, K., Ratra, B., Platt, S.R., Sugiyama, N., & Górski, K.M. 1999, ApJ, 525, 1

[60]Schlegel, D. J., Finkbeiner, D.P., & Davis, M. 1998, ApJ, 500, 525

[61]Shandarin, S.F., Feldman, H.A., Xu, Y., & Tegmark, M. 2001, astro-ph/0107136

[62]Simonetti, J.H., Dennison, B., & Topasna G.A. 1996, ApJ, 458, L1

[63]Smoot, G.F. 1998, astro-ph/9801121

[64]Stompor, R., et al. 2001, ApJ, submitted (astro-ph/0105062)

[65]Valls-Gabaud, D. 1998, PASP, 15, 111

[66]Veeraraghavan, S., & Davies, R.D. 1997, unpublished manuscript

[67]Wang, Y., & Mathews, G. 2000, ApJ, submitted (astro-ph/0011351)

[68]Weingartner, J.C., & Draine, B.T. 2000, ApJ, 553, 581

[69]Wu, J.-H.P., et al. 2001, astro-ph/0104248

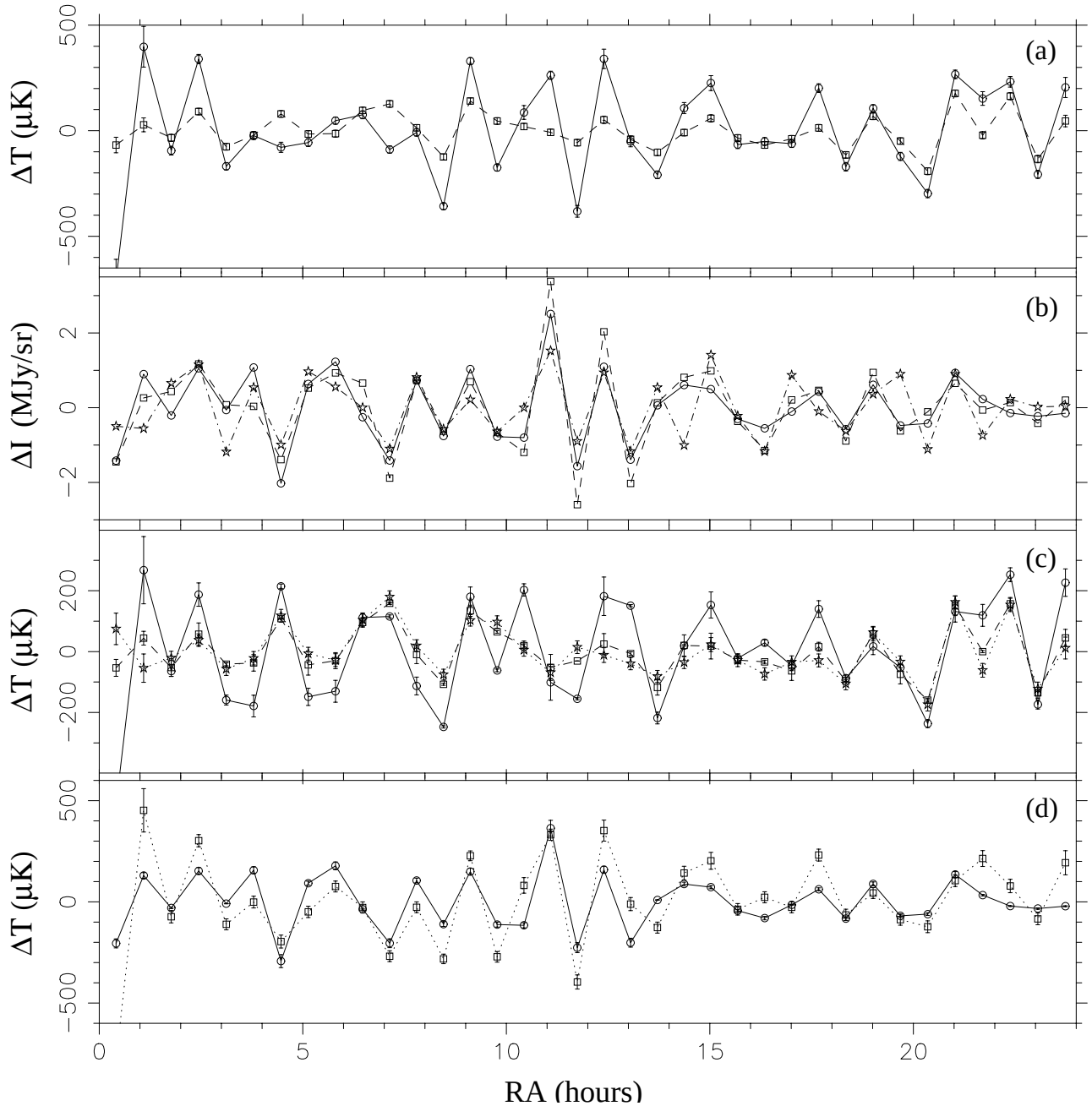

Fig. 1.— (*a*) OVRO 14.5 GHz data (open circles connected by solid lines) and 31.7 GHz data (open squares connected by dashed lines). (*b*) The 100 μm (open circles connected by solid lines), 60 μm $\times 10$ (open squares connected by dashed lines), and 12 μm $\times 20$ (stars connected by dot-dashed lines) dust emission templates after convolving with the OVRO beam and double differencing. (*c*) The OVRO 14.5 GHz data minus the 100 μm-correlated anisotropy (open circles connected by solid lines), the OVRO 31.7 GHz data minus the 12 μm-correlated fluctuations (open squares connected by dashed lines), and the CMB signal inferred on the basis of eq. (2) (stars connected by dotted lines). (*d*) The 100 μm-correlated anisotropy in the 14.5 GHz data (open circles connected by solid lines) and the foreground signal inferred using eq. (2) (open squares connected by dotted lines) at 14.5 GHz.

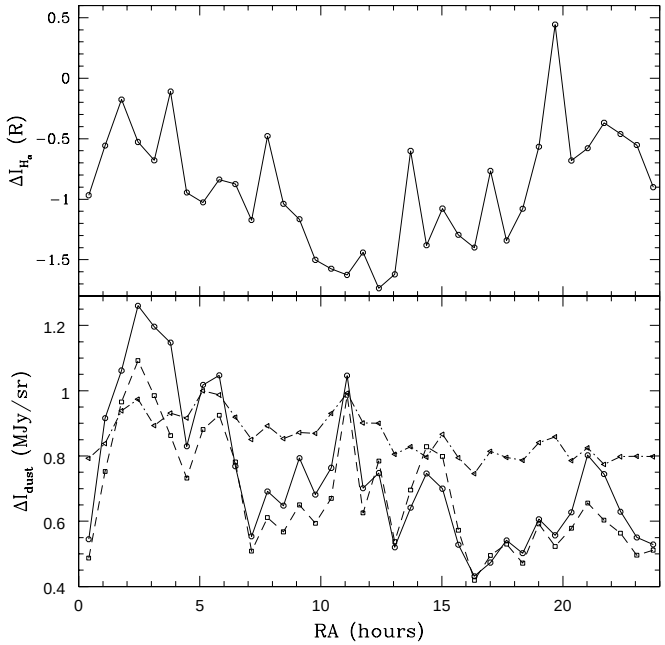

Fig. 2.— The top panel shows the H_α data (smoothed to $7'$) and the bottom panel shows the i100 template reduced by a factor of 8 (open circles connected by solid lines), the i60 template (empty squares connected by dashed lines), and the i12 template (empty triangles connected by dot-dashed lines) in the OVRO fields.

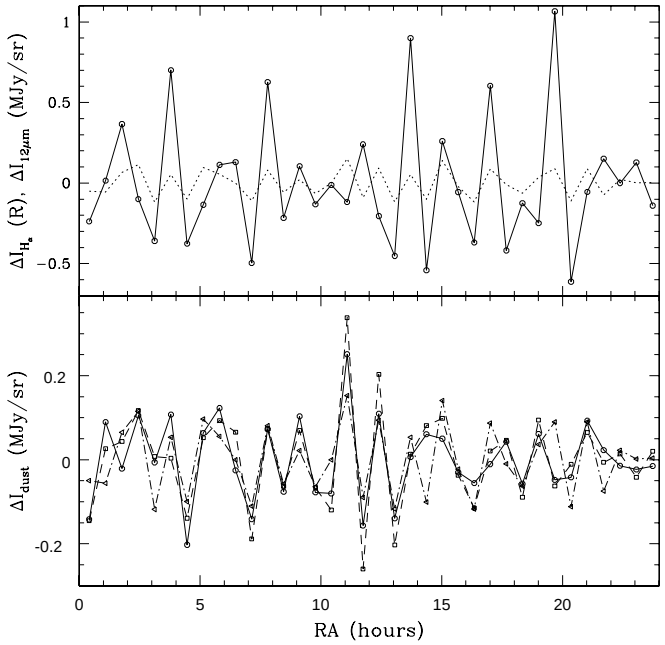

Fig. 3.— The top panel shows the H_α data (smoothed to $7'$, empty circles connected by solid lines) and the i12 template (dotted line) and the bottom panel shows the i100 template reduced by a factor of 10 (open circles connected by solid lines), the i60 template (empty squares connected by dashed lines), and the i12 template $\times 2$ (empty triangles connected by dot-dashed lines) in the OVRO fields after the OVRO doubles differencing.

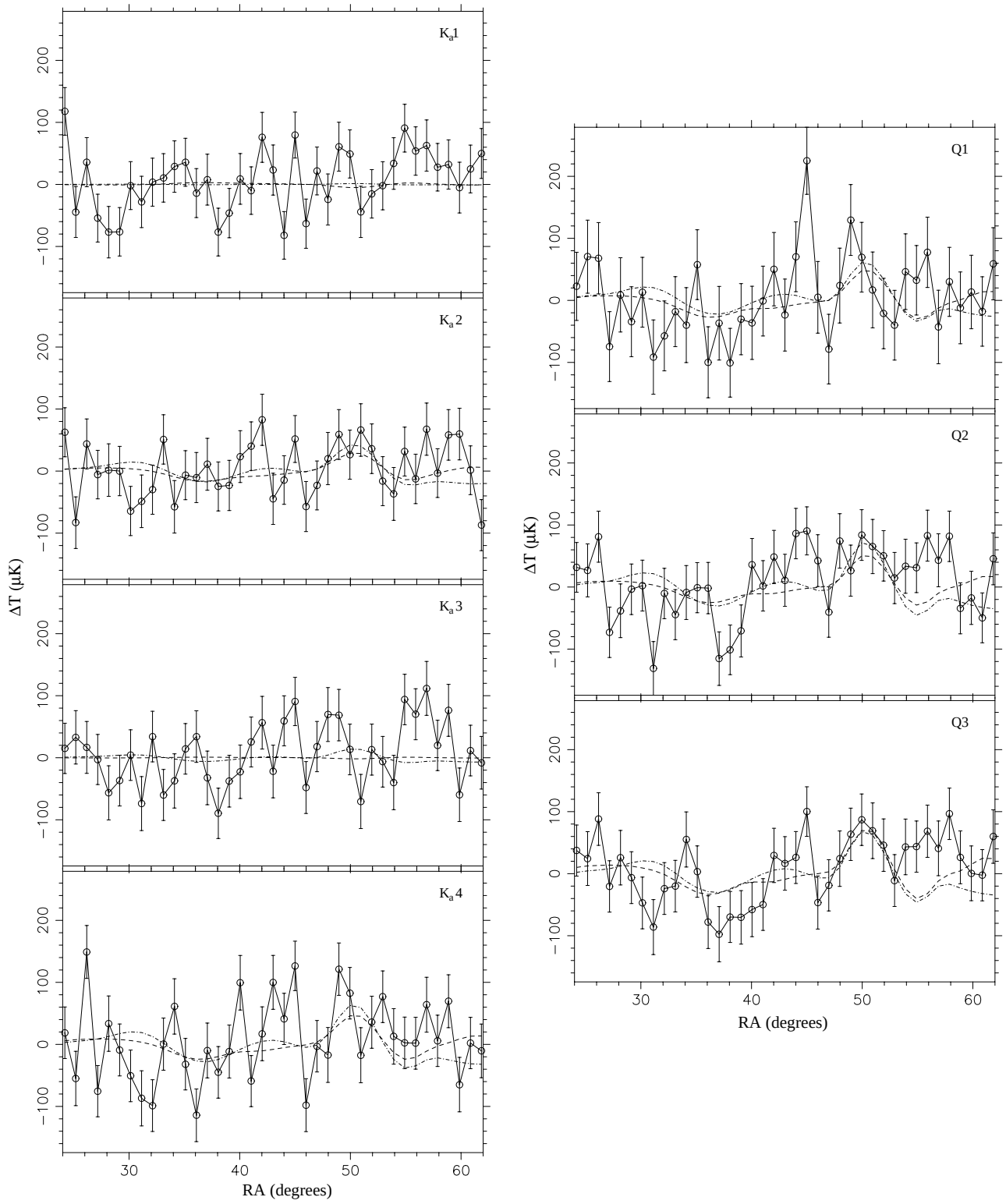

Fig. 4.— The SP94 data with 39 (of 43) pixels in each channel (open circles connected by solid lines show the K_a1, K_a2, K_a3, and K_a4 data in the four left panels, and $Q1$, $Q2$, and $Q3$ data in the three right panels), the 100 μm-correlated emission (dot-dashed curves), and the 12 μm-correlated emission (dashed curves). Each template is correlated individually with the data.

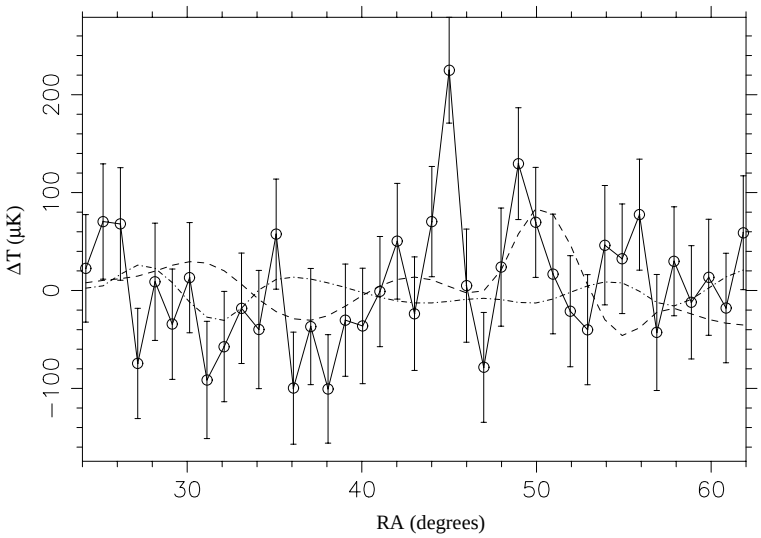

Fig. 5.— The SP94 data (39 of 43 pixels, open circles), the 100 μm correlated emission (dashed curve), and the H_α correlated emission (dot-dashed curve) all for channel $Q1$. The correlation method attributes a negative correlation to the H_α template (Table 6), and this figure shows that the inverted H_α curve and the dust emission curve have some common features.

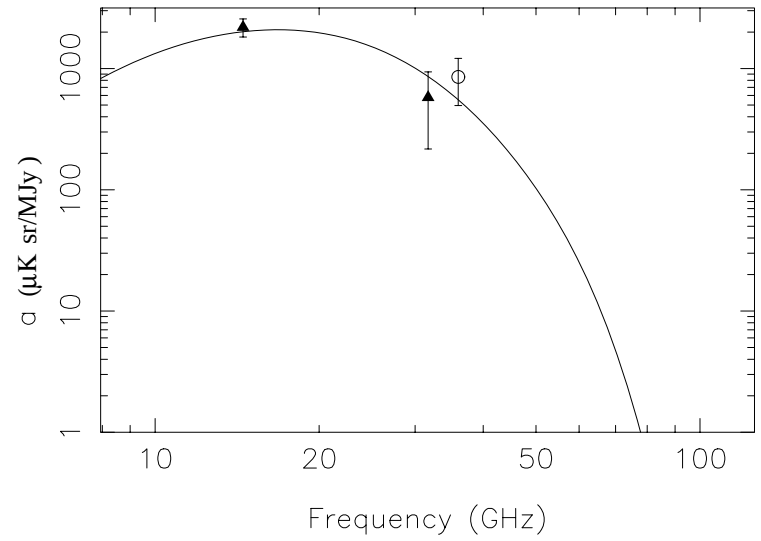

Fig. 6.— Correlation slope between CMB anisotropy data and the dust 12 μm template. Solid triangles show estimates obtained for the two OVRO frequencies, and the empty circle shows the estimated correlation slope for the SP94 data (when data from all channels are correlated together, with 39 of 43 pixels in each channel). The solid curve represents a spinning dust spectrum.